The Astrophysical Journal, 765:26 (11pp), 2013 March 1 doi:10.1088/0004-637X/765/1/26

DISSECTION OF Hα EMITTERS : LOW-z ANALOGS OF $z > 4$ STAR-FORMING GALAXIES

Hyunjin Shim[1,2] and Ranga-Ram Chary[3]
[1] Department of Earth Science Education, Kyungpook National University, Republic of Korea; hjshim@knu.ac.kr
[2] Spitzer Science Center, California Institute of Technology, MS 220-6, Pasadena, CA 91125, USA
[3] U.S. Planck Data Center, California Institute of Technology, MS 220-6, Pasadena, CA 91125, USA
Received 2012 May 1; accepted 2013 January 3; published 2013 February 13

ABSTRACT

Strong Hα emitters (HAEs) dominate the $z \sim 4$ Lyman-break galaxy (LBG) population. We have identified local analogs of these HAEs using the Sloan Digital Sky Survey. At $z < 0.4$, only 0.04% of the galaxies are classified as HAEs with Hα equivalent widths ($\gtrsim$500 Å) comparable to that of $z \sim 4$ HAEs. Local HAEs have lower stellar mass and lower ultraviolet (UV) luminosity than $z \sim 4$ HAEs, yet the Hα-to-UV luminosity ratio, as well as their specific star formation rate, is consistent with that of $z \sim 4$ HAEs, indicating that they are scaled-down versions of high-z star-forming galaxies. Compared to the previously studied local analogs of LBGs selected using rest-frame UV properties, local HAEs show similar UV luminosity surface density, weaker $D_n(4000)$ break, lower metallicity, and lower stellar mass. This implies that the local HAEs are less evolved galaxies than the traditional Lyman break analogs. In the stacked spectrum, local HAEs show a significant He II λ4686 emission line suggesting a population of hot, massive stars similar to that seen in some Wolf–Rayet galaxies. Low [N II]/[O III] line flux ratios imply that local HAEs are inconsistent with being systems that host bright active galactic nuclei. Instead, it is highly likely that local HAEs are galaxies with an elevated ionization parameter, either due to a high electron density or large escape fraction of hydrogen ionizing photons as in the case of Wolf–Rayet galaxies.

Key words: cosmology: observations – galaxies: evolution – galaxies: starburst

Online-only material: color figures, machine-readable table

1. INTRODUCTION

In attempts to understand the global star formation history over cosmic time, most conventional approaches start from the selection of high-redshift star-forming galaxies based on the different unique signatures in their spectral energy distribution (SED). Well-known examples are the Lyman break in the ultraviolet (UV) continuum, the Lyα emission line, the Balmer break in evolved stellar populations, and, more recently, the shape of the observed far-infrared SED, which shows a peak between ∼60 and 100 μm. The next step is to investigate their physical properties such as star formation rates (SFRs), stellar masses, and stellar populations using yardsticks calibrated in the local universe for which higher signal to noise and higher spatial resolution data are available, compared to the high-redshift galaxies being considered. By studying the local counterparts of high-redshift galaxies, it is possible to understand the physical trigger for star formation and its temporal evolution, and how physical parameters in the interstellar medium (ISM) affect observables that trace the star formation activity.

One well-known study is the investigation of local UV-luminous galaxies (UVLGs) as analogs of high-redshift Lyman-break galaxies (LBGs). Heckman et al. (2005) have studied the properties of FUV-luminous galaxies at $z \lesssim 0.3$ using the combination of *Galaxy Evolution Explorer* (*GALEX*) and Sloan Digital Sky Survey (SDSS) data. The FUV luminosities of the selected galaxies are greater than $2 \times 10^{10}\ L_{\odot}$, comparable to that of $z \sim 2$–3 LBGs. The number density of such UVLGs is 0.85% of all galaxies at $0.0 < z < 0.3$ (Hoopes et al. 2007). Hoopes et al. (2007) have shown that the specific SFR of UVLGs is correlated with their UV surface brightness, and the subset of compact UVLGs with the highest UV surface brightness (i.e., $I_{\rm FUV} > 10^9\ L_{\odot}\ {\rm kpc}^{-2}$; supercompact UVLGs) were considered to be the local counterparts to high-redshift LBGs in terms of their UV surface brightness, SFR, metallicity, and stellar mass.

These supercompact UVLGs, later denoted as Lyman break analogs (LBAs), have been studied in detail in the radio (Basu-Zych et al. 2007) and infrared (Overzier et al. 2009, 2011) which helps by providing a window into high-redshift star-forming environments in the local universe. For example, high spatial resolution studies of the morphologies of LBAs show clear evidence of merger-induced star formation (Overzier et al. 2008, 2010). In contrast, the signatures of mergers are not visible in the rest-frame UV observation of high-redshift galaxies. Ravindranath et al. (2006) demonstrated that only ∼30% of $z > 3$ galaxies show signatures of mergers. It is plausible that this derived fraction is a lower limit due to surface brightness dimming (Overzier et al. 2010). However, there is a theoretical suggestion that high-redshift star formation is preferentially governed by a supply of cold gas through cold flow accretion rather than merging (Dekel et al. 2009). It is not clear whether the "local counterparts" of high-redshift star-forming galaxies have a similar source of gas supply as distance galaxies, considering the difference in halo masses. Nevertheless, their similarities in observable properties are useful for evaluating whether the derived physical quantities for high-redshift galaxies, such as SFRs and dust obscuration, are robust. Thus, the key question is whether the UV-selected LBAs can be the representatives for high-redshift star-forming galaxy populations, reflecting their star formation characteristics as well as SFRs.

Recently, we have discovered that at least 70% of spectroscopically confirmed LBGs at $3.8 < z < 5.0$ show a flux density excess in *Spitzer* 3.6 μm over the stellar continuum, which is due to the redshifted Hα emission (Shim et al. 2011; Hα emitters, hereafter HAEs). The result is striking for two reasons: (1) strong nebular emission lines do affect broadband photometry and photometry-based SED fitting (e.g., Chary et al. 2005; Zackrisson et al. 2008; Capak et al. 2011; Schaerer & de Barros 2009), and (2) high-redshift galaxies show strong Hα emission, which implies an SFR that is as high, if not higher than

that inferred from their large UV luminosities. The estimated Hα equivalent widths (EWs) are in the range of 140–1700 Å, rarely seen in surveys of local galaxies. Despite the selection bias in favor of emission line sources that is associated with spectroscopic confirmation of LBGs, the value of 70% is unusually high. It suggests that there is a physical reason for this "strong Hα phase" that was previously not known. The high Hα-to-UV ratio and large Hα EW compared with the ages of the stellar population therein suggest that at least 50% of $z \sim 4$ HAEs prefer an extended star formation timescale rather than a burst-like, short (∼100 Myr) timescale. Therefore, such extended star formation histories should be included in the selection criteria for local counterparts of high-redshift star-forming galaxies.

In this paper, we selected local galaxies ($z < 0.4$) with Hα EW > 500 Å from the spectroscopic survey of the SDSS. We used the measured properties of these local HAEs to understand the properties of $z \gtrsim 4$ HAEs that dominate the high-redshift star-forming galaxy population. We investigated possible reasons for the origin of strong Hα emission in star-forming galaxies (e.g., presence of an active galactic nucleus (AGN), low metallicity, extended star formation histories, and dust extinction) by using spectroscopically derived values such as line indices and metallicities, as well as the UV-to-IR flux ratios. Throughout this paper, we use a cosmology with $\Omega_M = 0.27$, $\Omega_\Lambda = 0.73$, and $H_0 = 71\,\mathrm{km\,s^{-1}\,Mpc^{-1}}$.

2. THE LOCAL SAMPLE OF Hα EMITTERS

2.1. Local Hα Emitters

We selected objects with Hα EW larger than 500 Å from SDSS Data Release 7, using the MPA-JHU value-added catalog[4] (Kauffmann et al. 2003b; Brinchmann et al. 2004). After the Hα EW cut, we inspected each object individually in the SDSS image and spectrum. Extragalactic H II regions, which reside in the spiral arms of large $z \sim 0$ galaxies, are discarded. Due to the limited fiber size used in the SDSS spectroscopy (3″ diameter), the measured Hα EW corresponds to the EW in the central regions of an extended galaxy. Thus the galaxy-integrated Hα EW may be different if the line to continuum ratio changes dramatically in the outer parts of a galaxy. To ensure that gradients in EWs do not significantly affect our results, we excluded objects with half-light radii[5] larger than 3″. Finally, we are left with 299 galaxies (∼0.04%) out of 818,333 galaxies spectroscopically observed in SDSS DR7. We refer these galaxies as "local HAEs."[6]

As discussed above, the fiber spectra only sample the central regions for extended objects. Since it is possible that the stellar continuum may be less centrally concentrated compared with the line emission, aperture corrections are required as described in Brinchmann et al. (2004). Brinchmann et al. (2004) estimated the aperture correction of up to a factor of 10 to be applied to the SFRs and stellar mass values in the MPA-JHU catalogs, based on the likelihood distribution function $P(\mathrm{SFR}/L_i|\mathrm{color})$. Since we do not have clues on the spatial distribution of the line emission, we applied aperture correction on the line fluxes based on the assumption that the line contribution to the broadband magnitude remains the same outside the fiber. First, we convolved the SDSS spectrum with filter bandpasses and derived the synthetic *r*-band or *i*-band magnitudes within the 3″ fiber. At redshifts greater than 0.05, the Hα line falls within the Sloan *i*-band filter while at lower redshifts, the line would be in the Sloan *r*-band filter. This synthetic magnitude within the fiber was compared to the observed total (Petrosian) magnitude, and the ratio between the two was used in the aperture correction. We found that the median of the aperture correction factor is ∼1.5.

Table 1 lists the SDSS photo-object IDs, coordinates, Hα flux and EW, and other parameters for local HAEs. The Hα flux and EW are the observed values, not corrected for dust extinction nor aperture limitation. The analysis such as the derivation of Hα luminosity has been performed after applying aperture correction on the numbers presented in Table 1.

2.2. Ancillary Data Used

Most parameters used in this analysis are drawn either from the MPA-JHU value-added catalog and/or the SDSS pipeline. Stellar mass, metallicity, line fluxes, and EWs for significant emission lines, 4000 Å break $D_n(4000)$ in the MPA-JHU value-added catalog are obtained through spectral and/or multi-wavelength photometry fitting. Here we briefly describe how each parameter is derived in the MPA-JHU value-added catalogs.

Metallicities, i.e., the oxygen abundances, were derived following the method presented in Tremonti et al. (2004). All of the most prominent emission lines ([O II], Hβ, [O III], Hα, [N II], [S II]) were fitted simultaneously to $\sim 2 \times 10^5$ models for integrated galaxy spectra (Charlot & Longhetti 2001) with varying metallicity, ionization parameter, and dust-to-metal ratio. The median of the likelihood distribution of the metallicity was adopted as the metallicity of each galaxy. The stellar masses were derived based on the multi-wavelength photometry fitting, following the method described in Kauffmann et al. (2003b) and Salim et al. (2007). Template galaxy spectra were generated using the Bruzual & Charlot (2003) population synthesis code, with metallicity range spanning 0.1–2 $Z_\odot$ and stellar population age spanning 0.1 Gyr to the age of the universe. An exponentially decaying star formation history was assumed with random starbursts superimposed on the continuous star formation. Internal reddening and attenuation due to the intergalactic medium (IGM) are applied to the template galaxy spectra, and the resulting template spectra were convolved with SDSS passbands to produce broadband photometry in each filter. After calculating χ^2 of the fit, probability distributions for each parameters, such as the SFR, stellar mass, and dust attenuation, were constructed. Rather than finding single best-fit template, the MPA-JHU value-added catalog presents the median of the distribution of each parameter.

We derived the *GALEX* far- and near-ultraviolet (FUV/NUV) flux densities of local HAEs from *GALEX* Data Release 6. *GALEX* has a spatial resolution of ∼6″. Using a cross-identification radius of 3″, 266 HAEs among 299 (∼90%) are observed in at least one *GALEX* band. After matching, each case was visually examined to make sure that FUV or NUV emission is from the local HAE itself, not contaminated by nearby objects. The flux density limit differs depending on which *GALEX* survey the ultraviolet flux has been drawn from; however, on average, the flux density limits in the FUV (1500 Å) and NUV (2300 Å) are 5 μJy and 4 μJy at 1σ, respectively.

We also obtained mid-infrared (MIR; 3–22 μm) photometry for local HAEs from the *Wide-field Infrared Survey Explorer*

[4] http://www.mpa-garching.mpg.de/SDSS/DR7/

[5] For half-light radius, we used *r*-band half-light radius calculated through the exponential disk fitting in the SDSS pipeline.

[6] Please note that local HAEs comprise a subset of all spectroscopically targeted SDSS galaxies. They are distinct from the faint, emission line galaxies found in a narrow-band imaging surveys.

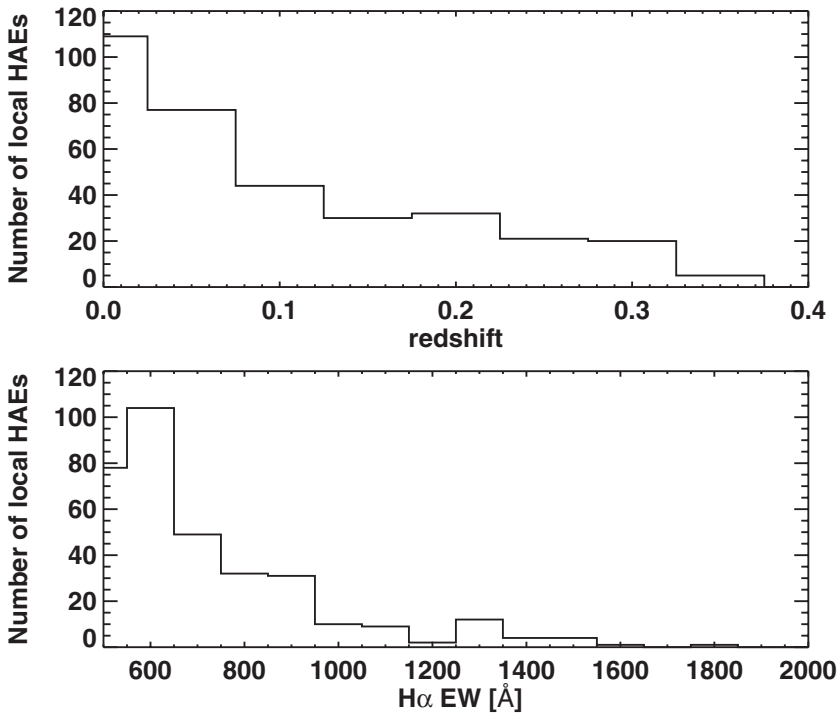

Figure 1. Redshift distribution (top) and Hα EW distribution (bottom) of 299 local HAEs. The EWs are the values in the observed frame, not in the rest frame.

Table 1
Local HAEs

SDSS ID	R.A.	Decl.	Redshift	Hα EW	f(Hα)	log $I_{\rm FUV}$	log SFR	log M_*	12+log[O/H]	D_n(4000)
587727179525783616	5.915092	−9.813522	0.053035	667.5	4001.6	8.447	0.481	8.608	8.149	0.8980
588015507661455435	6.104308	−1.066375	0.039368	611.7	1085.2	8.784	−0.610	...	8.007	0.9120
588015507661979813	7.409042	−1.204444	0.164415	752.8	865.7	9.116	0.675	...	8.155	0.8390
588015508199506053	8.835831	−0.746512	0.249825	503.4	773.8	8.819	0.920	...	8.255	0.9190
587740588411519244	9.582756	25.219419	0.311599	657.4	597.0	8.841	1.073	9.278	8.412	0.9694
587724199349387411	10.226349	15.569384	0.283232	636.7	478.4	8.939	0.873	9.240	...	0.8826
587724234248552589	10.653869	16.034079	0.247397	844.6	995.4	11.839	1.668	9.346	8.809	0.8554
587731186746196208	12.307815	0.400554	0.159282	896.6	580.6	9.116	0.256	8.942	7.673	0.7662
587731514215366775	16.450899	1.080542	0.329321	574.2	273.3	7.890	0.851	...	8.751	1.2555
587727180069142712	21.047823	−9.002034	0.229820	913.6	489.1	11.317	0.942	9.071	7.876	0.9508

Notes. Column 1: SDSS object ID. Column 2: Right Ascension (J2000). Column 3: Declination (J2000). Column 4: redshift. Column 5: Hα equivalent width in units of Å. Column 6: Hα line flux in units of 10^{-17} erg s^{-1} cm^{-2}. Column 7: FUV luminosity surface density in units of $L_\odot$ kpc^{-2}. FUV luminosity is derived using *GALEX* FUV magnitude, and is divided by $2\pi r_{\rm hl}^2$, while $r_{\rm hl}$ is half-light radius in SDSS u band. Column 8: log of the star formation rate in units of $M_\odot$ yr^{-1}. Column 9: log stellar mass in units of $M_\odot$. Column 10: 12+log[O/H]. Column 11: D_n(4000). Column 12: Comment for each object. We marked objects that are matched with Wolf–Rayet galaxies (Brinchmann et al. 2008) as "WR." Columns 5–6 and 8–11 are from the MPA-JHU value-added catalog for SDSS DR7.

(This table is available in its entirety in a machine-readable form in the online journal. A portion is shown here for guidance regarding its form and content.)

(*WISE*) all-sky data release (Cutri et al. 2012). Among 299 galaxies, 192 are detected in either *WISE* channel 3 (12 μm) or channel 4 (22 μm) with approximate flux density limits of $S_{12\,\mu{\rm m}} > 1$ mJy and $S_{22\,\mu{\rm m}} > 4.3$ mJy at the 5σ level. *WISE* channel 3 and channel 4 band fluxes are converted to the total infrared luminosities using bolometric corrections derived from model infrared galaxy templates (Chary & Pope 2010).

3. COMPARISON WITH OTHER GALAXIES

3.1. Comparison with $z \sim 4$ HAEs

Local HAEs are distributed at $0 < z < 0.4$, with more than half lying at $z < 0.1$ (Figure 1). Figure 2 shows how local HAEs and their $z \sim 4$ counterparts (Shim et al. 2011) compare with each other in terms of the luminosity, stellar mass, and the SFR. In Figure 2(a), we compare the Hα and FUV luminosity of local HAEs, $z \sim 4$ HAEs, and LBAs from Overzier et al. (2011). The Hα/FUV luminosity ratio of local HAEs is consistent to be ∼0.032 over the wide luminosity range. The dotted line is a linear fit to describe the correlation between the Hα and UV luminosity of local HAEs, with a slope close to unity. $z \sim 4$ HAEs also lie at the luminous end of such correlation, showing that Hα/FUV luminosity ratio of both local and $z \sim 4$ HAEs is very similar. On the other hand, local LBAs fall far below the fitted line, with an Hα/FUV luminosity ratio of ∼0.0063. Typical $z \sim 4$ HAEs are more luminous than the most luminous local HAEs by a factor of 10, therefore $z \sim 4$ HAEs are scaled-up versions of local HAEs.

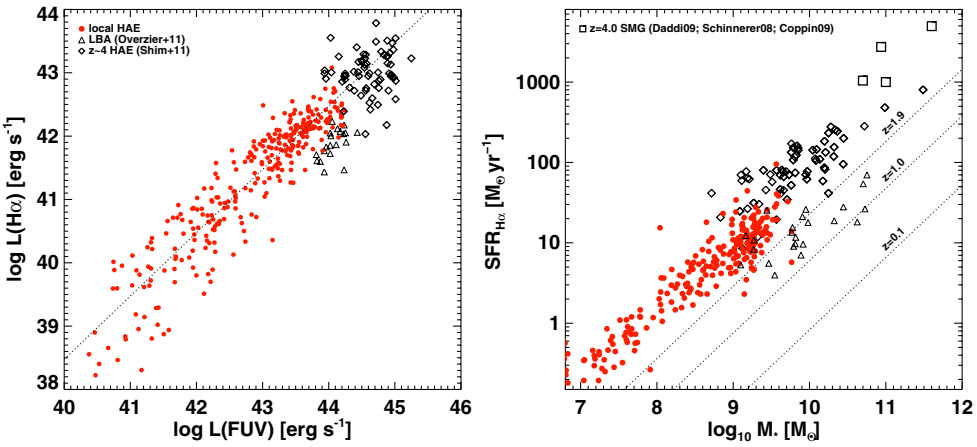

Figure 2. Left: comparison between Hα and FUV luminosity (λL_λ at 1500 Å) of local HAEs (filled circles), local Lyman break analogs (triangles; Overzier et al. 2011), and $z \sim 4$ HAEs (diamonds; Shim et al. 2011). The dotted line is a linear fit to describe L(Hα) vs. L(FUV) of local HAEs, and its slope value is almost unity (0.99). $z \sim 4$ HAEs lie along this line, implying that $z \sim 4$ HAEs are scaled-up versions of local HAEs. LBAs lie below the dotted line, suggesting that their Hα luminosity is on average lower than HAEs by a factor of three with the same UV luminosity. Right: comparison of SFR against stellar mass for local HAEs, LBAs, and $z \sim 4$ HAEs. The SFR is derived from the aperture-corrected (see Section 2.1) Hα luminosity, using the relationship in Kennicutt (1998). Overplotted dotted lines indicate SFR–M_* correlation of star-forming galaxies at different redshifts (Elbaz et al. 2007; Noeske et al. 2007; Daddi et al. 2007). $z \sim 4$ HAEs produce SFR per unit stellar mass comparable to $z = 2.8$–4.0 submillimeter galaxies (open squares; Daddi et al. 2009; Schinnerer et al. 2008; Coppin et al. 2009). Local HAEs show similar SFR per unit stellar mass as $z \sim 4$ HAEs, while LBAs lie well below the correlation. The high-mass end of the stellar mass distribution of local HAEs overlaps with the low-mass end for $z \sim 4$ HAEs at 10^9–10^{10} $M_\odot$.

(A color version of this figure is available in the online journal.)

In Figure 2(b), we compare the SFRs relative to the stellar mass of local HAEs, $z \sim 4$ HAEs, and LBAs. The Hα-based SFRs are derived assuming a Salpeter initial mass function (IMF) and a constant SFR following the same method used for $z \sim 4$ HAEs (Shim et al. 2011). The ratio of SFR to stellar mass is referred to as the specific SFR. Dotted diagonal lines in the figure show specific SFRs at different redshifts of star-forming main-sequence galaxies based on the literature (Elbaz et al. 2007; Noeske et al. 2007; Daddi et al. 2007). Local HAEs show Hα-based SFRs that are almost a factor of 30 higher than typical local star-forming galaxies of the same stellar mass, i.e., they show the elevated specific SFRs that are comparable to that of $z \sim 4$ HAEs and merger-driven high-redshift submillimeter galaxies. The stellar mass range sampled by local HAEs is on average lower than that of $z \sim 4$ HAEs. There is a significant overlap between local and $z \sim 4$ HAEs at 10^9–10^{10} $M_\odot$; yet a dominant fraction (~65%) of local HAEs appear to be small galaxies with stellar mass smaller than 10^9 $M_\odot$.

It is therefore clear that the Hα EW $>$ 500 Å selection identifies local galaxies that are similar in their specific SFRs to large Hα EW galaxies at $z \sim 4$ but with scaled-down SFRs and stellar masses. The Hα EW-based selection is more discriminatory than the luminosity cut in the single band, which can have strong selection effects due to the distance term. While a detailed investigation into the origin of strong Hα at $z > 4$ is challenging, local HAEs can be used to investigate the origin of strong Hα emission—the contribution from the AGN, anomalous physical properties.

Note that it is also possible that there could be $z \sim 4$ HAEs with Hα EW less than 500 Å. However, since our selection for high-redshift HAEs is based on the broadband photometric excess in the *Spitzer* 3.6 μm imaging data in the Great Observatories Origins Deep Survey fields (Shim et al. 2011) we are biased toward selecting the largest EW objects. Such large EW objects are also being found in small numbers at lower redshifts in wide-field spectroscopic surveys (Atek et al. 2011).

3.2. Comparison with Local UV-selected Star-forming Galaxies

We next compare local HAEs with previous local analogs of LBGs: UVLGs and LBAs, which are a subset of UVLGs. UVLGs and LBAs, selected based on either FUV luminosity or FUV surface luminosity density (Heckman et al. 2005; Hoopes et al. 2007; Overzier et al. 2009), have comparable FUV luminosity to that of high-redshift galaxies yet their Hα emission is significantly weaker. This implies that either the star formation history and/or the physical parameters related to star formation are likely to be different from that of high-redshift LBGs. Therefore, the LBAs are thought to be more analogous to the $z \sim 2$ galaxy population where the Hα EWs are correspondingly lower (Reddy et al. 2010; Erb et al. 2006) while the HAEs sample $z \sim 4$ galaxies.

Then what would be the reason for local HAEs being less luminous in FUV compared with $z \sim 4$ HAEs or LBAs? Figure 3 illustrates the distribution of Hα EW and UV surface brightness of local HAEs and UVLGs ($L_{\rm FUV} > 10^{10.3}$ $L_\odot$). The UV surface brightness is estimated at 1530 Å, i.e., the central wavelength of the *GALEX* FUV band. The surface brightness is calculated by dividing one-half the rest-frame 1530 Å luminosity[7] by the area of the galaxy encompassed within the half-light radius in the u band ($I_{\rm FUV} = L_{\rm FUV}/2\pi r_{50,u}^2$; Hoopes et al. 2007). For the half-light radius in the u band, we used the radius from the seeing-corrected exponential model fit calculated by the SDSS pipeline (`expRad`), which is consistent with the analysis of Hoopes et al. (2007). For galaxies larger than 2.″2, which would be resolved even in seeing-limited images, the Petrosian radius (`petroRad`) was used instead of the exponentially fitted radius. When FUV surface brightness is compared, local HAEs have as high FUV surface brightness as UVLGs and about half of the local HAEs may also classify as LBAs (shaded region in

[7] FUV magnitudes used in LBA studies (Hoopes et al. 2007) are from *GALEX* Data Release 2, and FUV magnitudes used in our analysis are from *GALEX* Data Release 6.

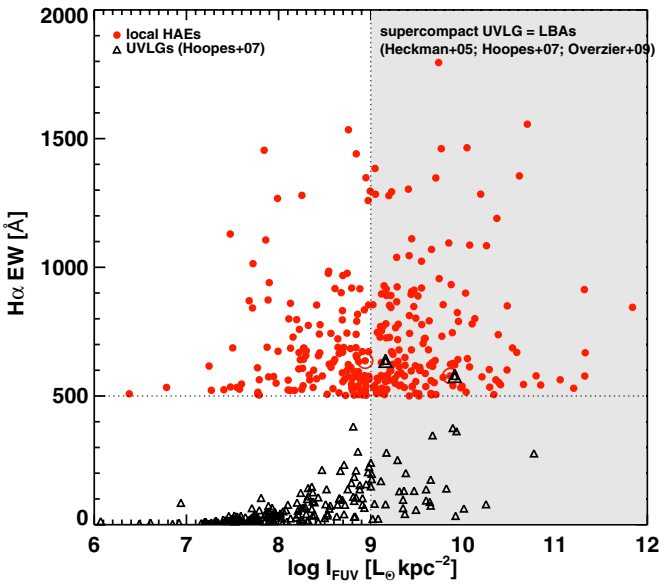

Figure 3. Comparison between the UV luminosity surface density and Hα EW of local HAEs and LBAs. LBAs are a subset of UV-luminous galaxies (UVLGs, $L_{\rm FUV} > 10^{10.3}\ L_{\odot}$; Heckman et al. 2005; Hoopes et al. 2007) that have relatively high UV surface luminosity ($I_{\rm FUV} > 10^{9}\ L_{\odot}$ kpc^{-2}). In this plot, local HAEs are plotted as filled circles, and UVLGs (Hoopes et al. 2007) are plotted as open triangles. Shaded region indicates the region where supercompact UVLGs, i.e., LBAs, fall. Although the total UV luminosity is not as high as that of LBAs, nearly 50% of the local HAEs have as high a UV surface luminosity as that of LBAs. Only two objects (symbols enclosed with larger symbols) are found to be overlapping between the local HAE and UVLG sample.

(A color version of this figure is available in the online journal.)

Figure 3) considering their compactness of the FUV emission. Their high UV luminosity surface density is mostly due to the small half-light radius of local HAEs rather than the value of their UV luminosity.

Many local HAEs show compact morphologies despite their redshift distribution being skewed toward lower redshift compared with UVLGs. The redshift distribution of UVLGs ranges between $z = 0.05$ and 0.3, while the redshift distribution of HAEs ranges between $z = 0.001$ and 0.35. As a result, the half-light radius of local HAEs is in general smaller than 5 kpc, while the half-light radius ($r_{50,u}$) ranges between 1 and 15 kpc for UVLGs. Because of this difference in $r_{50,u}$, the median UV surface brightness ($\langle I_{\rm FUV}\rangle$) of local HAEs ($10^{9}\ L_{\odot}$ kpc^{-2}) is higher than that of UVLGs ($10^{8}\ L_{\odot}$ kpc^{-2}). This shows that there exist a significant number of local starbursts with specific SFRs similar to that of high-redshift star-forming galaxies but which are missed in samples that use the total UV luminosity as the primary selection criterion.

Despite the similarity in UV surface brightness, the spectral features appearing in the composite spectrum of LBAs and local HAEs are significantly different. Figure 4 shows a comparison between the composite spectrum of LBAs and local HAEs (top), as well as the comparison between the composite spectrum of local HAEs and a single Wolf–Rayet galaxy, IC3591 (bottom). The composite spectrum is constructed by stacking the spectrum after normalizing to the continuum flux at 4800 Å. The composite spectrum of 197 local HAEs shows clear He II 4686 Å emission, He I 4471 Å and 4921 Å lines, and other forbidden lines such as [Fe III] 4658 Å, [Ar IV] 4711 Å, and 4740 Å lines. The [N II] emission at either 6548 Å or 6584 Å is relatively weak compared with Hα, and [O III] doublet at 5007 Å is strong compared with Hβ. The composite spectrum of 27 LBAs (Overzier et al. 2009) does not show any of these high ionization lines. The stellar continuum at 4000–6000 Å for local HAEs is slightly bluer than that for LBAs. When the optical stellar continuum is approximated using $F_{\lambda} \propto \lambda^{-\gamma}$, the slope γ for local HAEs is 3.9 while that for LBAs is 1.8, two times lower.[8] The bluer stellar continuum of local HAEs implies that local HAEs would be low-metallicity objects and/or they suffer less dust extinction compared with LBAs, which will be further discussed in Section 5.

3.3. Comparison with Wolf–Rayet Galaxies

We matched 299 local HAEs with the catalog of previously studied Wolf–Rayet galaxies (Zhang et al. 2007; Brinchmann et al. 2008). In total, 43 local HAEs (∼14%) are identified as Wolf–Rayet galaxies, which are specifically marked in Table 1. Besides these 43, we found that another 59 local HAEs show He II λ4686 emission with S/N ∼ 3, although they have no counterparts in the Wolf–Rayet galaxies catalog. The spectrum and the He II λ4686 EW of 59 galaxies are consistent with that of non Wolf–Rayet galaxies with He II emission line presented in Shirazi & Brinchmann (2012). For the remaining HAEs, we were able to construct a composite spectrum. At the bottom panel of Figure 4, we compare the composite spectrum of local HAEs (197 objects without the Wolf–Rayet signature in the individual spectrum; same as in Figure 4(a)) with the spectrum of a Wolf–Rayet galaxy IC 3591 (Brinchmann et al. 2008). The composite spectrum does not show the existence of a broad blue bump around 4686 Å typical of Wolf–Rayet galaxies, yet does show emission lines that require a high ionization field, as in Wolf–Rayet galaxies.

The origin of the He II 4686 Å line is unclear and has been discussed extensively in Thuan & Izotov (2005) and Shirazi & Brinchmann (2012). The former argue for radiative shocks while the latter present a range of scenarios including a population of hot, early-type stars due to stellar rotation. The strength of He II 4686 Å is known to be dependent on Hβ EW (Brinchmann et al. 2008; Shirazi & Brinchmann 2012). IC3591, compared here, has an Hβ EW of 263 Å (Hα EW = 1556 Å), thus it is one of the galaxies with the largest Hβ EWs among Wolf–Rayet galaxies. We do not find any significant evidence for the strength of Hα emission in the local HAEs being a preferential identifier of Wolf–Rayet galaxies. However, it appears that local HAEs are intermediate in their properties between Wolf–Rayet galaxies and LBAs in terms of their emission line strengths as well as the strength of the intrinsic ionizing photon field that is responsible for exciting the aforementioned lines.

4. He II EMISSION LINE

The He II 1640 Å emission line has long been suggested as a direct probe for hot Population III stars at high redshifts due to its high ionization potential of 54.4 eV (e.g., Schaerer 2003). Previous observations of high-redshift galaxies have only provided upper limits on He II 1640 Å (e.g., Dawson et al. 2007). In the local universe, the He II 4686 Å line is a distinguishing characteristic of Wolf–Rayet galaxies with hot, massive stars while X-ray binaries, strong shocks, low-level AGN activities, and stellar evolution model implemented with stellar rotation are also alternative origins for the line (Shirazi & Brinchmann 2012). Since the composite spectrum and ∼20% of the local

[8] The slope is determined for arbitrary F_{λ} units, thus the numbers should be used for relative comparison only.

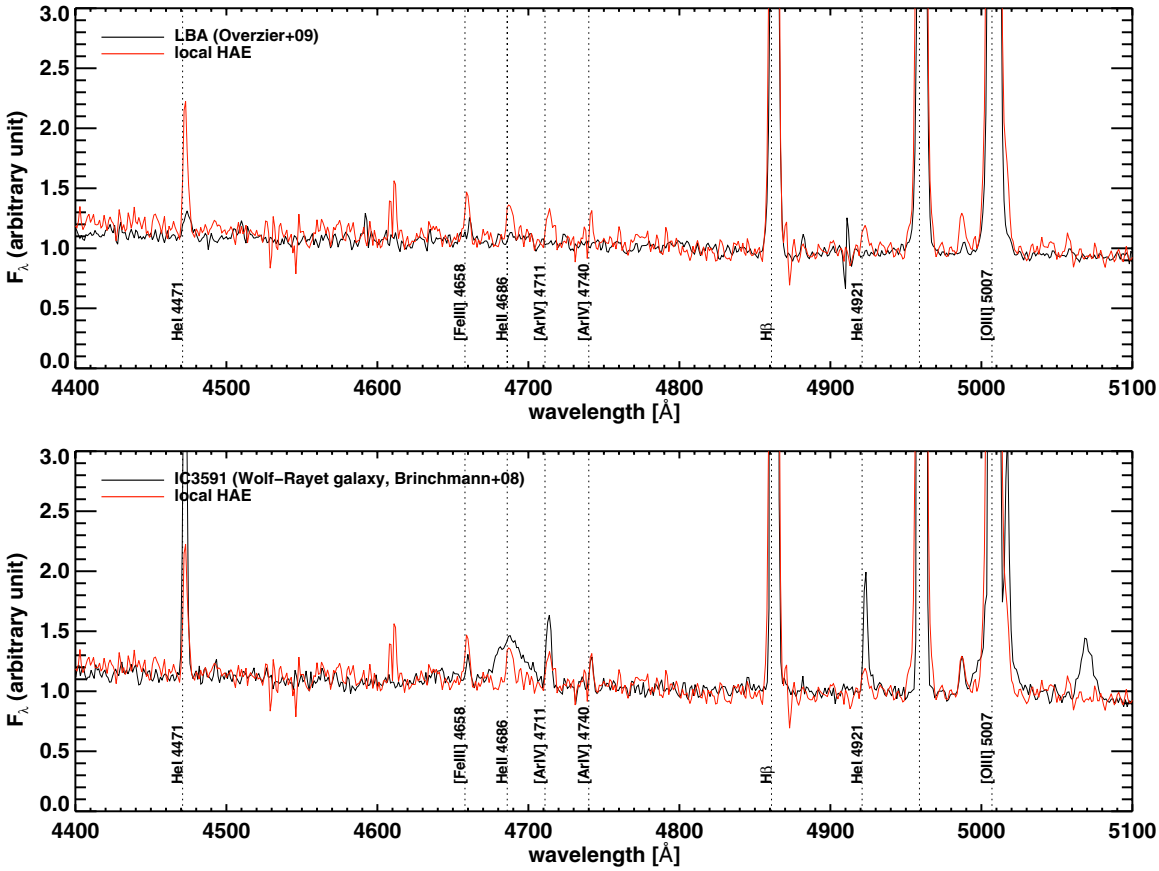

Figure 4. Top: comparison between the composite spectrum of 197 local HAEs that are not individually classified as Wolf–Rayet galaxies and the composite spectrum of 27 LBAs (Overzier et al. 2009). When making a composite spectrum, each spectrum was weighted using the continuum flux at 4800 Å. No evidence of spectral features indicating the existence of Wolf–Rayet stars (such as the blue bump around He II 4686 Å and/or He II 4686 Å line itself) was present in each of the individual spectra. The composite spectrum of HAEs does show the He II 4686 Å line. Other metal lines at high ionization stages, e.g., [Fe III] 4658 Å, [Ar IV] 4711 Å, 4740 Å also appear in the composite spectrum. Bottom: comparison between the composite spectrum of 197 local HAEs (same as above) and the spectrum of a single Wolf–Rayet galaxy IC3591 (chosen from Brinchmann et al. 2008; with Hβ EW of 263 Å). The composite spectrum of local HAEs shows several emission lines similar to Wolf–Rayet galaxies, including He recombination lines and high-order Fe and Ar lines, suggesting that the ionization field of local HAEs is comparable to that of Wolf–Rayet galaxies.

(A color version of this figure is available in the online journal.)

HAEs (59 out of 299) show He II 4686 Å emission line of S/N $\sim$ 3 in their individual spectrum, we investigated the ratio of He II 4686 to Hα line flux of local HAEs to get clues about the ratio between He-ionizing photons and H-ionizing photons in these systems. Considering that the local HAEs reflect star formation properties of $z \sim 4$ LBGs, the ratio of He-ionizing photons and H-ionizing photons would provide constraints for the detection of the He II 1640 Å line at $z \sim 4$.

Figure 5 shows the ratio between He II λ4686 flux and Hα flux for the individual (diamonds) and stacked HAEs (squares). In case of individually detected objects, we only plotted objects with S/N $>$ 7, clearly showing the narrow He II λ4686 line since it is difficult to discriminate nebular (narrow) He II line and stellar wind driven He II line if the S/N is only $\sim$3. He II 4686 Å emission line fluxes are measured by subtracting the stellar continuum through a simple linear fit and fitting a single Gaussian to the residual emission. In the stacking of the spectra, we divided 197 local HAEs into two bins of metallicity, based on the bimodal metallicity distribution illustrated in Figure 6. The size of each subsample is roughly the same ($\sim$100). Then the He II 4686 Å and Hα line fluxes are measured in the two composite spectra, one for metal-poor (point at metallicity 0.01) and the other for metal-rich (point at 0.002) galaxies. Overplotted shaded regions are the expected He II 4686/Hα ratio from the STARBURST99 population synthesis model for a range of stellar IMF, metallicity, and ionization parameters (T, N_e) of a 5 Myr old galaxy after an instantaneous starburst (Leitherer et al. 1999; Schaerer 2003).

The increase of ionization temperature, electron density, and the slope of IMF boosts up the He II 4686/Hα ratio, yet the effect is not significant. A temperature change from 5000 K to 20,000 K and an electron density change from 10^4 cm^{-3} to 10^6 cm^{-3} produces up to 50% change in the He II/Hα ratio. The effect of the IMF, including the mass range and slope, is limited to a factor of 2–3. For metal-poor local HAEs, the observed He II/Hα ratio is consistent with the expectation based on the Salpeter IMF with mass range of 1–200 $M_\odot$.

The two most dominant factors taking a role in the increase of He II/Hα ratio are metallicity and star formation history. As has been discussed in Schaerer (2003), metallicity strongly affects the ratio of hydrogen to helium ionizing photon output due to the increase in the effective stellar temperatures with decreasing metallicity. Thus, as metallicity decreases, the stellar population synthesis models result in a higher rate of hydrogen ionizing photons produced relative to the number of helium ionizing photons, which translates to a decreasing He II λ4686/Hα ratio. Due to the short lifetimes of very massive, hot Wolf–Rayet type

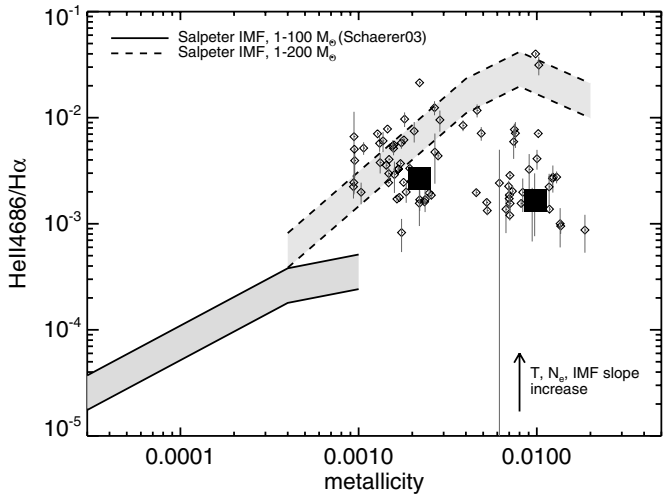

Figure 5. He II 4686 Å-to-Hα line flux ratio of local HAEs. Diamonds are local HAEs with He II 4686 Å detection in their individual spectra (including galaxies that are identified as Wolf–Rayet galaxies in Brinchmann et al. 2008). For local HAEs without individual He II detection, not classified as Wolf–Rayet galaxies, we stacked their spectra and derived He II/Hα ratio from the stacked spectrum (two filled squares). The shaded region indicates the expected range in He II/Hα ratio from the STARBURST99 population synthesis models (Leitherer et al. 1999; Schaerer 2003). A 5 Myr old population is assumed. The slope of the IMF was varied from -0.4 (top of the shaded region) to -2.3 (bottom of the shaded region), the ionization temperature T was varied between 5000 K and 20,000 K, while the electron density N_e was varied between 10^4 cm^{-3} and 10^6 cm^{-3}. While the slope of the IMF, mass limit of the IMF, and the parameters regarding ionization environment (T, N_e) have relatively small effects on the observed He II/Hα ratio, the metallicity appears to be the most dominant factor that affects the He II/Hα line flux ratio. The model He II 4686 to Hα ratio has been reddened assuming $A_V = 0.2$ mag.

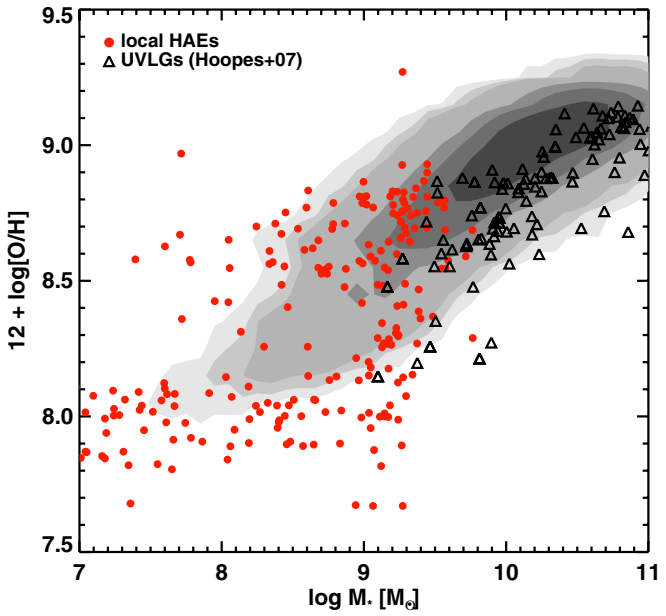

Figure 6. Mass–metallicity relation of the local HAEs (filled circles). Gas-phase metallicity and stellar mass for local HAEs are from the MPA-JHU value-added catalog constructed using SDSS DR7. Stellar mass has been derived based on the photometry fits (methods from Kauffmann et al. 2003a; Salim et al. 2007). Gas-phase metallicity has been derived through the emission line modeling (Tremonti et al. 2004; Brinchmann et al. 2004). Local HAEs are plotted over the contours that show the density distribution of all SDSS DR7 galaxies that have been spectroscopically observed. Also compared here are UVLGs (triangles; Hoopes et al. 2007; $L_{\rm FUV} > 10^{10.3}\ L_\odot$), among which the most compact galaxies are classified as LBAs.

(A color version of this figure is available in the online journal.)

stars that are responsible for the helium ionizing photons, after 5 Myr from the onset of star formation, the He II intensity drops while Hα still remains elevated due to the existence of late B and A stars. On the other hand, if the star formation history of a galaxy is continuous, the He II/Hα ratio is low before the evolution of Wolf–Rayet stars, and after few Myr, both helium ionizing photons and hydrogen ionizing photons are produced at a constant rate (Leitherer et al. 1999). Therefore, if we compare the same 5 Myr old galaxy with instantaneous starburst and with continuous star formation when other parameters are exactly the same, the He II/Hα ratio would be higher for a galaxy with an instantaneous starburst.

Local HAEs with low metallicity (point at $\sim$0.002 in Figure 5) show the He II/Hα ratio consistent with a 5 Myr old stellar population, with the scatter within the allowed IMF and the ionization parameter range. At higher metallicity (point at $\sim$0.01), the observed He II/Hα ratio is lower than the expectation from 5 Myr old stellar population, suggesting that these HAEs prefer continuous star formation history rather than instantaneous burst. This is consistent with the preferred star formation history of $z \sim 4$ HAEs being continuous star formation (Shim et al. 2011).

Since we have demonstrated that local HAEs are analogs of $z \sim 4$ HAEs, we can estimate the He II λ1640 emission line flux from the Hα line flux of $z \sim 4$ HAEs, and assess the feasibility of detecting the He II λ1640 emission line in the spectroscopy of high-redshift galaxies[9]. Using the He II λ4686/Hα ratio of $\sim$0.002 (values measured in the stacked spectrum of low-metallicity local HAEs) and the median Hα luminosity of 10^{43} erg s^{-1} (Shim et al. 2011), the He II λ1640 line flux of $z \sim 4$ HAEs is expected to be 1.6×10^{-18} erg s^{-1} cm^{-2}. The effect of dust attenuation is neglected in this calculation. This is comparable but slightly lower than the He II upper limits of Lyα emitters (LAEs) at $z \sim 4$ ($<2 \times 10^{-18}$ erg s^{-1} cm^{-2}; Dawson et al. 2007). However, it should be noted that the relationship between LAEs and HAEs is currently ambiguous. The HAEs in Shim et al. (2011) are typical spectroscopically confirmed LBGs, whereas the LAEs are preferentially lower mass systems. Therefore to detect the He II λ1640 emission line in $z > 4$ HAEs, future observations should aim to achieve line flux limits down to $5\sigma \sim 10^{-18}$ erg s^{-1} cm^{-2}.

[9] The adopted ratio of He II 4686 to He II 1640 for this calculation is 6.5 (Osterbrock & Ferland 2006).

5. PROPERTIES OF LOCAL HAEs: ORIGINS OF STRONG Hα EMISSION

In Shim et al. (2011), we presented several possible reasons for the origin of the unusually strong Hα emission in the $z \sim 4$ HAEs, especially compared to other star formation tracers such as the UV continuum. The possible factors that drive strong Hα emission in high-z HAEs are (1) extinction properties that are different with that of local starbursts (i.e., extinction curve steeper in UV), (2) young stellar population ages and star formation history, (3) low metallicity, and (4) a stellar IMF with an overabundance of massive stars. The AGNs were ruled out as a plausible explanation based on the non-detection of the $z \sim 4$ HAEs in the deep *Chandra* X-ray data. In the previous section, we investigated the stellar IMF and star formation history, reaching the conclusion that the IMF does not need to be top-heavy to explain the observed He II/Hα ratio and a continuous star formation history is preferred. In

this section, we investigate each of the other possible scenarios for the origin of strong Hα emission in local HAEs using the diagnostic properties of SDSS spectroscopy and UV-to-MIR photometry.

5.1. Low Metallicity

Figure 6 shows gas-phase metallicities (12 + log[O/H]) and stellar masses of local HAEs from the MPA-JHU value-added catalog for SDSS DR7. The metallicity distribution of local HAEs is clearly bimodal, one peak at 12 + log[O/H] ∼ 8.6 and another peak at 12 + log[O/H] ∼ 8.0. Half of the local HAEs are located at the low end of the stellar mass distribution ($M_* < 10^9\ M_\odot$) and the low end of the metallicity distribution (12 + log[O/H] < 8.3). This is different from the case for UVLGs (Hoopes et al. 2007). Almost all UVLGs are more massive than $10^9\ M_\odot$ and have metallicity 12+log[O/H] > 8.3. The most metal-rich UVLGs are almost super-solar metallicity. The higher metallicity of UVLGs, the higher masses compared with local HAEs, and the absence of He II in the spectra of UVLGs suggest that UVLGs are likely to be a more evolved system than HAEs.

The [O III]/Hα ratios of local HAEs do not appear to correlate with Hα EWs with a median line flux ratio of [O III]/Hα ∼ 1.7. Thus, it is difficult to assess the connection between the gas-phase metallicity and the Hα EW. However, there is a clear trend where the lower metallicity systems appear to show a factor of two weaker [O III] line flux corresponding to their Hα line flux than the highest metallicity systems in the sample.

The low metallicity of local HAEs is also reflected in their [N II]λ6584/Hα ratios, i.e., local HAEs show weak [N II] emission compared with Hα. The median value of the observed [N II]λ6584/Hα is ∼0.08, far less than the conventional [N II]λ6584/Hα = 0.3 for local star-forming galaxies (Gallego et al. 1997). This places local HAEs well to the left of the line that divides starbursts and AGNs in the BPT diagram (Baldwin et al. 1981; Kauffmann et al. 2003a; Kewley et al. 2001). Figure 7 shows the location of local HAEs in the [O III] 5007/Hβ vs. [N II]6584/Hα diagram. The location of the local HAEs shows that it is unlikely that the strong Hα emission is due to the AGN. The divider for AGN and starburst (e.g., Kauffmann et al. 2003a) is based on the AGN modeling with metallicity equal to or larger than solar metallicity. Thus, low-metallicity AGNs, if they exist, might overlap with the location of HAEs (Groves et al. 2006). The ratio between He II λ4686 and Hβ is an alternative probe of AGN-dominated system (e.g., Shirazi & Brinchmann 2012), and all but two local HAEs have He II λ4686/Hβ ratio as low as that of starburst-dominated system. Therefore, the possibility of AGNs as a dominant origin of strong Hα is again eliminated.

The location of the local HAE population in the BPT diagram partly depends on the gas-phase metallicity (12 + log[O/H]), i.e., galaxies with lower metallicity show even less [N II]/Hα ratio than galaxies with higher metallicity (the different symbols of different colors trace the metallicity in Figure 7). Also shown for comparison are the location of Wolf–Rayet galaxies (Brinchmann et al. 2008) and UVLGs (Hoopes et al. 2007) in the BPT diagram. Significant numbers of either Wolf–Rayet galaxies or UVLGs are classified as AGN-dominated systems, while most of Wolf–Rayet galaxies and/or UVLGs show higher [N II]/Hα compared with local HAEs. Again as in Figure 6, the BPT diagram suggests that UVLGs, as well as Wolf–Rayet galaxies in general, are on average more evolved than local HAEs.

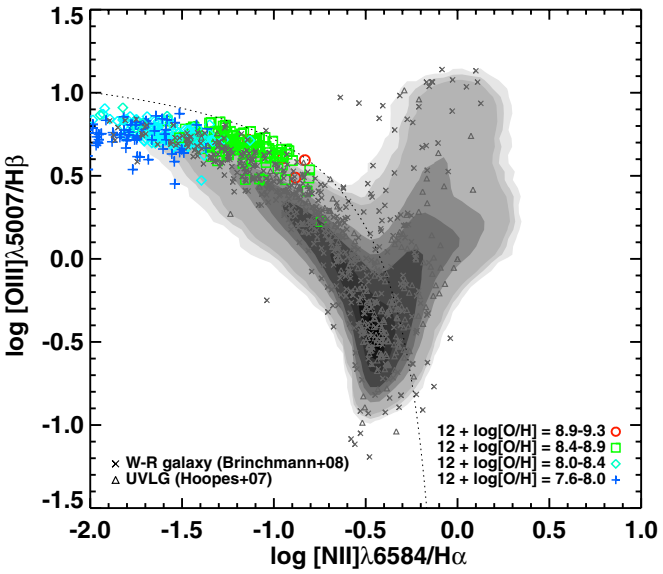

Figure 7. BPT diagram (Baldwin et al. 1981) of local HAEs. Contours show the density distribution of all emission line galaxies in SDSS DR7. The dotted line represents the criterion that divides AGN-dominated galaxies (upper right) and star-formation-dominated galaxies (lower left) as defined in Kauffmann et al. (2003b). Local HAEs with different gas-phase metallicities are plotted using different symbols: red circles correspond to the most metal-rich galaxies (8.9 < 12 + log[O/H] < 9.3) and the metallicity decreases as the symbols change to green squares, cyan diamonds, and blue plus symbols. Also shown are the locations of Wolf–Rayet galaxies (crosses; Brinchmann et al. 2008) and UVLG-LBAs (triangles; Hoopes et al. 2007) in the BPT diagram.

(A color version of this figure is available in the online journal.)

Another interesting point in Figure 7 is that local HAEs lie at the highest boundary of the entire local galaxy population showing the highest [O III]/Hβ ratios. It means that there exists a non-negligible offset between the median ridge line of [O III]/Hβ ratio for local galaxies and that of local HAEs (∼1.6 in [O III]/Hβ line flux; Kewley & Dopita 2002). This offset is also reported for star-forming galaxies at $z > 2$ (Erb et al. 2006). Brinchmann et al. (2008) suggest that this offset from the BPT ridge line is closely related to the amount of star formation, it being roughly proportional to the Hα EW. High-redshift galaxies lying well above the ridge line are producing unusually large amounts of stars compared with their stellar mass, i.e., showing larger specific SFR, and this displacement can be achieved by increasing the ionization parameter (the ratio of the volume densities of ionizing photons and particles). Again, the increase of the ionization parameter depends on the ratio of ionizing photons, electron densities, and the geometry of H II regions, which determines whether the H II regions are density-bound or ionization-bound: Brinchmann et al. (2008) suggest higher electron densities and larger escape fraction of hydrogen ionizing photons as two major reasons for this offset in the BPT diagram. These can be also applicable to local HAEs, considering that local HAEs show a clear displacement in the BPT diagram. Thus, local HAEs appear to be excellent laboratories for the study of high-z star-forming environments and a measure of the ionizing photon flux from these objects would validate the origin of the unusual [O III]/Hβ ratios.

5.2. Stellar Age

In Shim et al. (2011), we demonstrated that the most dominant factor that drives the "strong Hα phase" is the star formation history of high-z star-forming galaxies. The ubiquity of strong Hα emission and the evolved stellar population indicate that

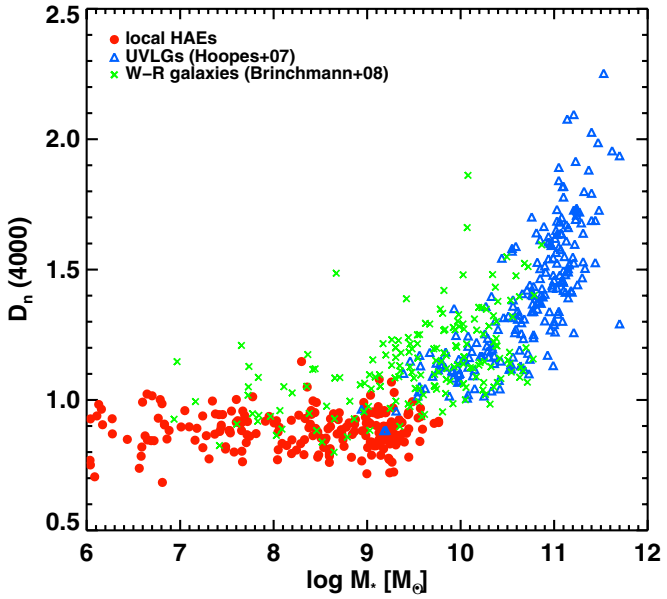

Figure 8. 4000 Å break strengths (D_n (4000)) vs. stellar mass for local HAEs (filled circles), UVLGs (triangles; Hoopes et al. 2007), and Wolf–Rayet galaxies (crosses; Brinchmann et al. 2008). Local HAEs tend to be young and less massive compared with LBAs and W–R galaxies.

(A color version of this figure is available in the online journal.)

$z \sim 4$ star-forming galaxies appear to display continuous star formation history rather than burst-like star formation. At $z \sim 4$, the interpretation corroborates a star formation mechanism that is powered by a continuous gas supply such as cold gas accretion from the filaments into massive halos. Short-timescale events such as mergers would be stochastic and would suggest a strong Hα emitting phase for only 10% of the galaxies.

In order to study the ages of the stellar population in local HAEs we compare the strength of the 4000 Å break, D_n (4000), of these galaxies and UVLGs in Figure 8. Local HAEs sample a broad range of stellar masses covering 10^6–10^{10} $M_\odot$, a broad range of FUV luminosity covering 10^8–10^{11} $L_\odot$, yet in terms of D_n (4000), local HAEs are a relatively homogeneous population with D_n (4000) < 1.0. There is no correlation between D_n (4000) and stellar mass or FUV luminosity for HAEs. On the other hand, there is a positive correlation between D_n (4000) and the stellar mass of UVLGs: Older UVLGs appear to be more massive.

Wolf–Rayet galaxies appear to show properties between those of HAEs and UVLGs. The D_n (4000) of Wolf–Rayet galaxies is not as homogeneously small as HAEs. Furthermore, Wolf–Rayet galaxies are more massive than HAEs but less massive than UVLGs. Wolf–Rayet galaxies therefore appear to be older than HAEs of the same UV luminosity based on the strength of their 4000 Å break but are younger than the majority of UVLGs. It is as expected that Wolf–Rayet galaxies are older than local HAEs since the evolution of Wolf–Rayet stars strongly depends on the metallicity. Thus, considering that the composite spectrum of HAEs does show emission lines observed in Wolf–Rayet galaxies, such as He II lines, which suggest some similarity in their ionizing photon field, a zeroth-order conclusion is that HAEs evolve into Wolf–Rayet galaxies as they age and become metal-enriched. Since the D_n (4000) features arise due to absorption lines from ionized metals, the difference in D_n (4000) between two populations suggests the possibility that HAEs are at an earlier lower metallicity stage of evolution than Wolf–Rayet galaxies. To summarize, HAEs are likely to be at the initial stage of burst, based on the strong Hα, narrow He II line, and the absence of a D_n (4000) break. After a few Myr, as the metallicity evolves with the starburst, Wolf–Rayet stars appear with strong stellar winds. These galaxies may then end up after a few hundreds Myr as LBAs that still produce stars continuously.

5.3. Dust Obscuration in Local HAEs

Hα line fluxes and EWs considered in this paper are not corrected for dust attenuation. In this subsection, we present and compare several different extinction indicators of local HAEs, constraining their extinction properties. We also assess the possible implications for the shape of the differential extinction as a function of wavelength.

5.3.1. Extinction Indicators

The first observable extinction indicator is the UV spectral slope β. β is derived based on the assumption that the spectrum of star-forming galaxies in the UV wavelength range are well described by a power law ($f_\lambda \propto \lambda^\beta$). We assumed that this power-law approximation is applicable to the rest-frame wavelength range of 1500/(1 + z)Å–2300/(1 + z)Å, covered by the *GALEX* FUV and NUV bands. Then we converted the (FUV − NUV) color to a spectral slope β using the following relation:

$$\beta_{\rm FUV-NUV} = (m_{\rm FUV} - m_{\rm NUV})/0.464 - 2.0, \quad (1)$$

where $m_{\rm FUV}$ and $m_{\rm NUV}$ indicate the *GALEX* magnitudes in the FUV and NUV bands corrected for Galactic extinction. The low S/N of the local HAEs in the *GALEX* FUV and NUV bands propagates into the derived β. The derived $\beta_{\rm FUV-NUV}$ is highly uncertain in most cases; 40% of all objects have uncertainty higher than 0.2 in β.

The above assumption is accurate for objects with $z < 0.1$. However, for objects at $z > 0.1$, the Lyα emission line may contaminate the observed flux density in the *GALEX* FUV band, which makes the broadband colors bluer and induces some uncertainty in β. For standard Case B recombination, the Lyα to Hα line ratio is a factor of ∼10. We estimate that in the most extreme case, this would bias the FUV flux upward by 20% and thereby affect the UV slope β by 0.4. We have not applied this correction because we do not know the true strength of the Lyα line in these sources and because of the fact that the effect of *GALEX* photometric uncertainty itself on β values is typically larger. Furthermore, the comparison with UVLGs and LBAs is more straightforward since those studies chose not to apply the correction as well.

The next extinction indicator is the flux ratio between hydrogen recombination lines that traces the different extinction at the wavelengths corresponding to the lines. Here, we present the Balmer line ratio $F_{\rm H\alpha}/F_{\rm H\beta}$ as the extinction indicator. Following Calzetti et al. (2000), the color excess of the nebular gas, $E(B-V)_{\rm gas}$, is calculated by comparing the observed Balmer line ratios with the intrinsic (i.e., unobscured) Balmer line ratios:

$$E(B-V)_{\rm gas} = \frac{2.5}{k(\lambda_1) - k(\lambda_2)} \log_{10} \frac{F_i^{\lambda_1}/F_i^{\lambda_2}}{F_o^{\lambda_1}/F_o^{\lambda_2}}. \quad (2)$$

Here, $F_i^{\lambda_1}/F_i^{\lambda_2}$ is the intrinsic line ratio, $F_o^{\lambda_1}/F_o^{\lambda_2}$ is the observed line ratio, and $k(\lambda)$ is an extinction value at the

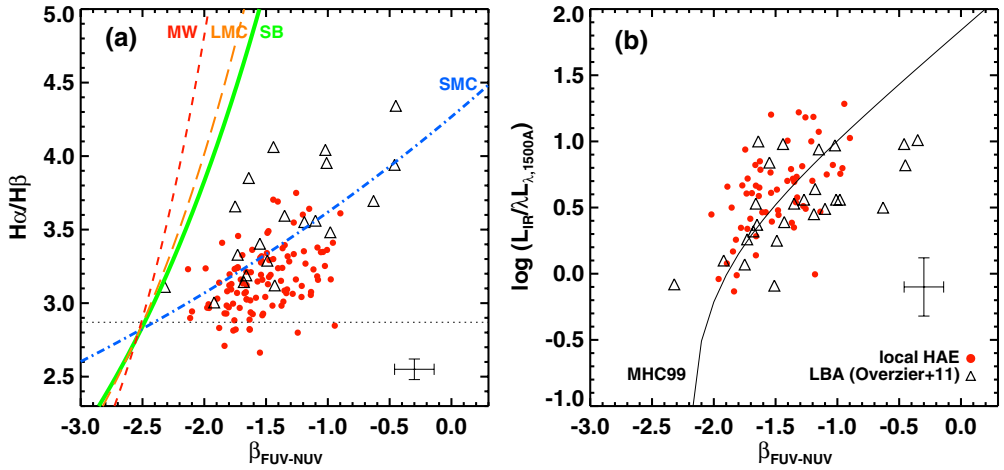

Figure 9. (a) Balmer line ratio (Hα/Hβ) vs. UV spectral slope β of local HAEs (filled circles) and LBAs (triangles; Overzier et al. 2011). UV slope β is derived using the *GALEX* FUV − NUV colors (see the text for details), and Hα/Hβ ratio is derived from the MPA-JHU catalog. Dotted horizontal line indicates $F_{\rm H\alpha}/F_{\rm H\beta} = 2.87$, the unobscured Balmer line flux ratio for case-B recombination with $T = 10^4$ K (Osterbrock & Ferland 2006). Overplotted tracks indicate Hα/Hβ vs. β expected from different dust extinction/attenuation laws (Allen 1976; Fitzpatrick 1986; Prévot et al. 1984; Calzetti et al. 2000). (b) IR-to-UV luminosity ratio vs. UV spectral slope β of local HAEs and LBAs. The overplotted line is the empirical IR-to-UV ratio vs. β relationship for local starbursts (Meurer et al. 1999).
(A color version of this figure is available in the online journal.)

corresponding wavelength described by the applied extinction curve. Based on the Case B recombination at $T = 10^4$ K (Osterbrock & Ferland 2006), the intrinsic Balmer line ratio is $F_{\rm H\alpha}/F_{\rm H\beta} = 2.87$.

Finally, the ratio between IR luminosity and UV luminosity can be used as a third extinction indicator, assuming that the IR luminosity is proportional to the entire unobscured stellar radiation. We derived IR luminosities of local HAEs using the *WISE* photometry in channels 3 and 4 (12 μm and 22 μm, respectively). By matching the coordinates of local HAEs to the *WISE* all-sky data release catalog (Cutri et al. 2012), we found 192 objects with robust counterparts. These objects do not have nearby neighbors within 3″ that could possibly contaminate the MIR flux density. We used IR SED templates of IR galaxies with different IR luminosities (Chary & Pope 2010): Each IR luminosity template was redshifted to the corresponding redshift of the object and the template that best explains the observed 12 μm and 22 μm flux density was determined, while the IR luminosity of the object was derived to be the IR luminosity associated with the best-fit template. IR luminosity of local HAEs ranges between $1.4 \times 10^8\,L_\odot$ and $7.6 \times 10^{11}\,L_\odot$. We compared $L_{\rm IR}$ with $L_{\rm UV}$, i.e., λL_λ at 1530 Å as defined in the previous section, and used $L_{\rm IR}/L_{\rm UV}$ as an extinction indicator.

The results for dust extinction using these three techniques are described in the next subsection.

5.3.2. Extinction Curve Differences in UV Wavelengths

Figure 9 illustrates the comparison between the three extinction indicators for local HAEs and LBAs. Figure 9(a) shows that there exists a positive correlation between UV slope β and $F_{\rm H\alpha}/F_{\rm H\beta}$, which is naturally expected from the fact that both quantities are providing independent measures of obscuration. Considering large uncertainties in β due to the large magnitude errors in both FUV and NUV bands, we only plotted objects with NUV magnitudes brighter than 19 mag and magnitude errors in FUV and NUV bands less than 0.1 mag.

For the same β, the flux ratio $F_{\rm H\alpha}/F_{\rm H\beta}$ of LBAs is higher than that of HAEs. One possibility is that the ISM temperature in LBAs and HAEs is different, with the latter having higher gas temperatures, which affect the recombination rate by a factor of 1.3. This would be consistent with the higher ultraviolet surface density seen in the HAEs compared with LBAs. The alternate interpretation is that this is a result of dust extinction. For a fixed $\beta_{\rm FUV-NUV}$, LBAs show larger dust extinction than HAEs, which implies that the UV dust extinction curve is steeper in HAEs than in LBAs. This is more consistent with the extinction curve seen in the Small Magellanic Cloud (SMC), which due to its low metallicity is thought to have an overabundance of large grains relative to small grains (Weingartner & Draine 2001). Recently, Wild et al. (2011) suggested that the UV slope in the extinction curve depends on the specific SFR of a galaxy, i.e., galaxies with large specific SFR have a higher fraction of dust that is more centrally concentrated, and thus have steeper UV slope. This is also consistent with the comparison between LBAs and HAEs, while HAEs have higher SFR than LBAs with the same stellar mass.

In Figure 9(b), we present the IR-to-UV luminosity ratio for local HAEs. Since the HAEs appear to be young galaxies while LBAs being relatively evolved, the IR-to-UV ratio of LBAs is expected to be smaller than that of HAEs since the fraction of stellar radiation that is absorbed by dust and re-radiated in the IR decreases as the galaxy evolves. The observed relation between the IR-to-UV ratio and UV spectral slope β for local HAEs lies above the expected line for local star-forming galaxies (Meurer et al. 1999) or that of LBAs, confirming the idea that young HAEs have stronger intrinsic UV radiation fields and thereby emit more strongly in the IR. Still, the uncertainties related to the derivation of $L_{\rm IR}$ and $\beta_{\rm FUV-NUV}$ are large. The addition of far-infrared continuum flux is needed to reduce the uncertainties in $L_{\rm IR}$. To constrain the extinction curve shape in UV wavelengths in more detail, the accuracy in $\beta_{\rm FUV-NUV}$ should also be improved with higher precision UV spectrophotometry, which disentangles the contribution of the Lyα line from the broadband photometry.

6. SUMMARY

In this paper, we have studied the extremely rare, local analogs of $z \sim 4$ star-forming galaxies from SDSS DR7. It has recently

been demonstrated in Shim et al. (2011) that 70% of $z \sim 4$ galaxies have strong Hα EWs and are HAEs. Therefore, unlike previous studies that selected local analogs based solely on their UV properties, we used the criterion Hα EW > 500 Å to select among the local galaxy population. At $z < 0.4$, the number fraction of such strong HAEs is only 0.04%. Local HAEs are less luminous by an order of magnitude in both Hα and UV luminosities compared with $z \sim 4$ HAEs. However, the Hα-to-UV luminosity ratio as well as the specific SFRs of local HAEs are very similar to those of high-redshift HAEs. This supports the argument that local HAEs are scaled-down versions of $z \sim 4$ star-forming galaxies.

In contrast, previously studied UV-selected local analogs of high-redshift LBGs, the LBAs, are distinct in their physical properties from HAEs at any redshift. The UV-selected analogs show a factor of five lower Hα EW, higher metallicity, and higher stellar mass than the HAEs. At least 50% of local HAEs show comparably high FUV surface brightness as that of LBGs and LBAs. However, the FUV surface brightness does not appear to depend on Hα EW. Unlike the LBAs, the composite spectrum of local HAEs shows strong, but narrow helium lines that are observed in Wolf–Rayet galaxies, raising the possibility that the ionization field in local HAEs is comparable to that of Wolf–Rayet galaxies that contain a large number of hot, massive stars.

Fifty percent of local HAEs show low metallicity of 12 + log[O/H] $\sim$ 8.0, close to $\sim$0.1 $Z_{\odot}$, which is less than that of the UV-selected LBAs. This is consistent with the fact that HAEs are less massive by at least an order of magnitude than the LBAs. The low metallicities are also reflected in their low observed [N II]/Hα ratio. The low [N II]/Hα ratio, high [O III]/Hβ ratio, and low He II λ4686/Hβ ratio indicate that local HAEs are not likely to be contaminated by AGN-dominated systems. Moreover, the strong [O III] emission that displaces local HAEs from the ridge line of BPT diagram can be explained by a high ionization parameter, which requires either higher electron densities and/or large escape fraction of hydrogen ionizing photons. If the large escape fraction is demonstrated through observational data, HAEs could be the clue to understanding the reionization of the IGM at high redshift.

Most HAEs are unusually young with $D_n(4000) < 1$. This is one of the largest differences between the properties of HAEs and Wolf–Rayet galaxies; the latter predominantly showing $D_n(4000) > 1$, suggesting a more evolved stellar population. The extinction indicator Hα/Hβ of local HAEs suggests that HAEs display an extinction curve steeper than normal star-forming galaxies and more similar to that of the SMC. The origin of this difference in extinction curve is not clear, with the most likely reason being the lower metallicities, as well as the high specific SFR, in these galaxies.

We thank the referee, J. Brinchmann, for his insightful comments and valuable suggestions that improved the paper. H.S. was supported by Kyungpook National University Research Fund, 2012. This publication makes use of data products from the *Wide-field Infrared Survey Explorer*, which is a joint project of the University of California, Los Angeles, and the Jet Propulsion Laboratory/California Institute of Technology, funded by the National Aeronautics and Space Administration.

REFERENCES

Allen, C. W. 1976, Astrophysical Quantities (3rd ed.; London: Athlone)
Atek, H., Siana, B., Scarlata, C., et al. 2011, ApJ, 743, 121
Baldwin, J. A., Phillips, M. M., & Terlevich, R. 1981, PASP, 93, 5
Basu-Zych, A. R., Schiminovich, D., Johnson, B. D., et al. 2007, ApJS, 173, 457
Brinchmann, J., Charlot, S., White, S. D. M., et al. 2004, MNRAS, 351, 1151
Brinchmann, J., Pettini, M., & Charlot, S. 2008, MNRAS, 385, 769
Bruzual, G., & Charlot, S. 2003, MNRAS, 344, 1000
Calzetti, D., Armus, L., Bohlin, R. C., et al. 2000, ApJ, 533, 682
Capak, P., Mobasher, B., Scoville, N. Z., et al. 2011, ApJ, 730, 68
Charlot, S., & Longhetti, M. 2001, MNRAS, 323, 887
Chary, R.-R., & Pope, A. 2010, arXiv:1003.1731
Chary, R.-R., Stern, D., & Eisenhardt, P. 2005, ApJL, 635, L5
Coppin, K. E. K., Smail, I., & Alexander, D. M. 2009, MNRAS, 395, 1905
Cutri, R. M., et al. 2012, VizieR Online Data Catalog, 2311, 0
Daddi, E., Dannerbauer, H., Stern, D., et al. 2009, ApJ, 694, 1517
Daddi, E., Dickinson, M., Morrison, G., et al. 2007, ApJ, 670, 156
Dawson, S., Rhoads, J. E., Malhotra, S., et al. 2007, ApJ, 671, 1227
Dekel, A., Birnboim, Y., Engel, G., et al. 2009, Natur, 457, 451
Elbaz, D., Daddi, E., Le Borgne, D., et al. 2007, A&A, 468, 33
Erb, D. K., Steidel, C. C., Shapley, A. E., et al. 2006, ApJ, 647, 128
Fitzpatrick, E. L. 1986, AJ, 92, 1068
Gallego, J., Zamorano, J., Rego, M., & Vitores, A. G. 1997, ApJ, 475, 502
Groves, B. A., Heckman, T. M., & Kauffmann, G. 2006, MNRAS, 371, 1559
Heckman, T. M., Hoopes, C. G., Seibert, M., et al. 2005, ApJL, 619, L35
Hoopes, C. G., Heckman, T. M., Salim, S., et al. 2007, ApJS, 173, 441
Kauffmann, G., Heckman, T. M., Tremonti, C., et al. 2003a, MNRAS, 346, 1055
Kauffmann, G., Heckman, T. M., White, S. D. M., et al. 2003b, MNRAS, 341, 33
Kennicutt, R. C. 1998, ARA&A, 36, 189
Kewley, L. J., & Dopita, M. A. 2002, ApJS, 142, 35
Kewley, L. J., Heisler, C. A., & Dopita, M. A. 2001, ApJS, 132, 37
Leitherer, C., Schaerer, D., Goldader, J. D., et al. 1999, ApJS, 123, 3
Meurer, G. R., Heckman, T. M., & Calzetti, D. 1999, ApJ, 521, 64
Noeske, K. G., Faber, S. M., Weiner, B. J., et al. 2007, ApJL, 660, L47
Osterbrock, D., & Ferland, G. 2006, Astrophysics of Gaseous Nebulae and Active Galactic Nuclei (2nd ed.; Sausalito, CA: Univ. Science Books)
Overzier, R. A., Heckman, T. M., Kauffmann, G., et al. 2008, ApJ, 677, 37
Overzier, R. A., Heckman, T. M., Schiminovich, D., et al. 2010, ApJ, 710, 979
Overzier, R. A., Heckman, T. M., Tremonti, C., et al. 2009, ApJ, 706, 203
Overzier, R. A., Heckman, T. M., Wang, J., et al. 2011, ApJL, 726, L7
Prévot, M. L., Lequeux, J., Prévot, L., Maurice, E., & Rocca-Volmerange, B. 1984, A&A, 132, 389
Ravindranath, S., Giavalisco, M., Ferguson, H. C., et al. 2006, ApJ, 652, 963
Reddy, N. A., Erb, D. K., Pettini, M., Steidel, C. C., & Shapley, A. E. 2010, ApJ, 712, 1070
Salim, S., Rich, R. M., Charlot, S., et al. 2007, ApJS, 173, 267
Schaerer, D. 2003, A&A, 397, 527
Schaerer, D., & de Barros, S. 2009, A&A, 502, 423
Schinnerer, E., Carilli, C. L., Capak, P., et al. 2008, ApJL, 689, L5
Shim, H., Chary, R.-R., Dickinson, M., et al. 2011, ApJ, 738, 69
Shirazi, M., & Brinchmann, J. 2012, MNRAS, 421, 1043
Thuan, T. X., & Izotov, Y. I. 2005, ApJS, 161, 240
Tremonti, C. A., Heckman, T. M., Kauffmann, G., et al. 2004, ApJ, 613, 898
Weingartner, J. C., & Draine, B. T. 2001, ApJ, 548, 296
Wild, V., Charlot, S., Brinchman, J., et al. 2011, MNRAS, 417, 1760
Zackrisson, E., Bergvall, N., & Leitet, E. 2008, ApJL, 676, L9
Zhang, W., Kong, X., Li, C., Zhou, H.-Y., & Cheng, F.-Z. 2007, ApJ, 655, 851